Fission and the *r*-process nucleosynthesis of translead nuclei in neutron star mergers

Samuel A. Giuliani [1,*] Gabriel Martínez-Pinedo,[2,3,4,†] Meng-Ru Wu,[5,6,7,‡] and Luis M. Robledo[8,9,§]

[1]*Department of Physics and Astronomy and NSCL/FRIB Laboratory, Michigan State University, East Lansing, Michigan 48824, USA*
[2]*GSI Helmholtzzentrum für Schwerionenforschung, Planckstraße 1, 64291 Darmstadt, Germany*
[3]*Institut für Kernphysik (Theoriezentrum), Department of Physics, Technische Universität Darmstadt,
Schlossgartenstraße 2, 64298 Darmstadt, Germany*
[4]*Helmholtz Forschungsakademie Hessen für FAIR, GSI Helmholtzzentrum für Schwerionenforschung, Planckstrae 1, 64291 Darmstadt,
Germany*
[5]*Institute of Physics, Academia Sinica, Taipei, 11529, Taiwan*
[6]*Institute of Astronomy and Astrophysics, Academia Sinica, Taipei 10617, Taiwan*
[7]*Physics Division, National Center for Theoretical Sciences, 30013 Hsinchu, Taiwan*
[8]*Center for Computational Simulation, Universidad Politécnica de Madrid, Campus de Montegancedo, 28660 Madrid, Spain*
[9]*Departamento de Física Teórica and CIAFF, Universidad Autónoma de Madrid, 28049 Madrid, Spain*

We study the impact of fission on the production and destruction of translead nuclei during the *r*-process nucleosynthesis occurring in neutron-star mergers. Abundance patterns and rates of nuclear energy production are obtained for different ejecta conditions using three sets of stellar reaction rates, one of which is based on microscopic and consistent calculations of nuclear masses, fission barriers, and collective inertias. We show that the accumulation of fissioning material during the *r* process can strongly affect the free neutron abundance after the *r*-process freeze-out. This leads to a significant impact on the abundances of heavy nuclei that undergo α decay or spontaneous fission, affecting the radioactive energy production by the ejecta at timescales relevant for kilonova emission.

I. INTRODUCTION

Sixty years after the seminal works of B[2]FH and Cameron [1,2], where the rapid neutron capture process (*r* process) was first indicated as the main mechanism responsible for the production of the heaviest elements observed in the universe, the GW170817 gravitational wave signal [3] and its associated AT 2017gfo electromagnetic (EM) counterpart [4] provided the first evidence that *r*-process nucleosynthesis occurs in neutron star mergers (NSM) [5–8]. This evidence arose from the observed optical and near-infrared emissions, which were found to be consistent with a quasithermal transient known as kilonova or macronova powered by the radioactive decay of freshly synthesized *r*-process nuclei [9–12]. However, whether NSM are the main astrophysical site contributing the production of *r*-process elements in the Galaxy remains an open question [13]. This is because despite the large amount of information extracted from the multimessenger observations, the detailed composition of the ejected material is still unclear (so far, the only element identified in the ejecta is strontium [14]). The near-infrared kilonova emission that was observed at timescales of several days is consistent with predictions assuming a significant presence of lanthanides (mass fraction $\gtrsim 10^{-2}$) in the ejecta [15,16], but the exact range of the produced nuclei or whether there was a possible presence of heavier elements has not yet been determined. In this context, future observations of late-time ($\gtrsim 10$ d) kilonova light curves showing signatures related to the decay of particular nuclei, together with improved kilonova emission modeling, would thus provide invaluable information to further progress in our understanding of the origin of *r*-process elements [17–19].

Both future observations as well as improved theoretical yield predictions are urgently required. From the nuclear physics side, one aspect that must be addressed is the sensitivity of the abundances of long-lived nuclei to nuclear properties and their impact on kilonova light curves. The presence of uranium and thorium in metal-poor stars, as well as in the solar system, indicates that if NSM are a major contributor to the production of *r*-process nuclei, the *r*-process path therein must reach the region of actinides. Therefore, it is likely that fission happens during and/or after the *r* process. Previous studies have shown that the kilonova light curves, particularly at late times, depend on the amount of translead nuclei, e.g., those in the mass range $222 \leqslant A \leqslant 225$ and $A = 254$, whose yields depend on the adopted nuclear mass model [18,20–22], and/or the fission probabilities of heavy nuclei during their decay to stability [17,23,24]. However, crucial understanding of the role played by fission in the production and destruction of translead nuclei during and after the *r* process is still lacking.

*giuliani@nscl.msu.edu
†g.martinez@gsi.de
‡mwu@gate.sinica.edu.tw
§luis.robledo@uam.es

In this paper, we study the production of translead nuclei during the *r*-process nucleosynthesis using three different sets of stellar reaction rates and trajectories representing three different ejecta conditions in NSM. In particular, we focus on the role that fission plays in the destruction of very heavy elements and the implications for the electromagnetic transients powered by the radioactive decay of the synthesized nuclei. The paper is organized as follows: Sec. II discusses the nuclear properties underlying the stellar reactions rates and the different trajectories employed in this work; Sec. III reports the main results concerning the evolution of total abundances and nuclear energy release rates; finally, Sec. IV summarizes the main findings and outlines future works.

II. METHOD

One of the major challenges in *r*-process nucleosynthesis calculations is to study the impact of nuclear properties in the abundance patterns and kilonova light curves. The difficulties arise from the fact that the nuclear reaction network calculations simulating the *r*-process nucleosynthesis require the knowledge of nuclear masses, reaction rates, and decay properties for several thousands of nuclei placed between the valley of stability and the neutron drip line. Due to the fact that changes in the nuclear abundances are nonlocal and that there are processes such as fission that connect very different regions of the nuclear chart, it is in general very challenging to determine the nuclear properties that affect the production of particular nuclear species.

Rather critical is the case of fission, where the experimental data suitable for *r*-process calculations is particularly scarce. As a result, only few papers so far addressed the impact of fission during the *r*-process nucleosynthesis [20,23,25–35]. The aim of this paper is to improve the understanding of the role played by fission in the production of translead nuclei and its possible relevance for kilonova by employing a recently developed set of reaction rates and fission properties based on the Barcelona-Catania-Paris-Madrid (BCPM) energy density functional (EDF) [36,37].

The BCPM neutron-induced reaction rates, α-decay rates, and spontaneous fission lifetimes were obtained using the nuclear masses, fission barriers, and collective inertias predicted by the BCPM EDF [38]. This is one of the few attempts to derive a set of reaction rates and nuclear decay properties suited for *r*-process calculations from a consistent nuclear input (see also Ref. [23,24,31]). Since β-decay rates are not available for this functional we employed the finite range droplet model (FRDM) β-decay rates [39] and derived a set of β-delayed fission rates based on BCPM fission barriers and an estimate of the FRDM β strength function from the neutron emission probabilities. For nuclei with $Z < 84$, where fission is not expected to play a relevant role, we use the neutron capture rates based on the FRDM masses [40] as detailed in Ref. [20].

In the literature, two sets of reaction rates have been widely used in *r*-process calculations involving fission. The rates from Panov *et al.* [41] are based on a combination of FRDM nuclear masses [42] and Thomas-Fermi (TF) fission barriers [43] (see, e.g., Ref. [20,33]). More recently, the Brussels

group derived a set of reaction rates [44] based on Skyrme-EDF calculations using the HFB-24 mass model [45] and the HFB-14 fission properties [46] (see, e.g., Refs. [31,32]). In the following, we will refer to these two set of reaction rates as FRDM+TF and HFB14, respectively, and we will use them as reference models to assess the impact of fission properties of translead nuclei in the *r*-process nucleosynthesis. This requires the additional calculation of stellar reaction rates for photodisintegration, which we obtained from the neutron capture rates by detailed balance.

Figure 1 shows the FRDM+TF, HFB14, and BCPM predictions of the highest fission barrier (B_f), the difference between fission barrier and β-decay Q value ($B_f - Q_\beta$) [1] and the difference between fission barrier and neutron separation energy ($B_f - S_n$) for nuclei with $Z \geqslant 84$ [2]. These quantities provide a rough estimation of the stability of each nucleus against the different fission modes: spontaneous fission, β-delayed fission, and neutron-induced fission, respectively. Evidently, the smaller these values are, the larger the fission probabilities become. Looking at nuclei close to the neutron dripline, it is clear that BCPM and HFB14 predict systematically larger fission barriers compared to TF, particularly in the vicinity of the $N = 184$ shell closure. In Sec. III we will show how these properties, fission barriers, neutron separation energies, and Q_β values, determine the amount of material that can be accumulated in the heaviest region of the *r*-process nucleosynthesis.

Regarding the astrophysical scenario, we focused our study in the *r*-process nucleosynthesis occurring in NSM. In order to reach conclusions that are independent of the astrophysical conditions, we employed three trajectories representing different kind of ejecta conditions. The evolution of their mass density, temperature, entropy, and the free neutron number density n_n are plotted in Fig. 2. The ones labeled by (dynamical) hot and (dynamical) cold are trajectories produced by general-relativistic merger simulation [47] that were used in previous studies discussing the role of masses in shaping the *r*-process abundances [20]. Both of them have initially low entropies of $\approx 1\ k_B$ per nucleon and very low electron fraction per nucleon $Y_e \lesssim 0.05$. The difference between them is that the dynamical hot ejecta expand slower than the dynamical cold one. In the former, the nuclear energy release during the *r* process is able to reheat the ejecta to temperatures $\gtrsim 1$ GK, while only ≈ 0.2 GK for the latter (see Fig. 1 and Eq. (8) in Ref. [20]). Consequently, an $(n, \gamma) \rightleftarrows (\gamma, n)$ equilibrium

---

[1]We stress that the BCPM and HFB14 β-delayed fission rates are based on β-strength functions, and hence Q_β values, predicted by FRDM. For consistency the bottom (middle) center panel of Fig. 1 shows the difference between the BCPM (HFB14) fission barriers and FRDM Q_β values, since the latter were used to determine the maximum β-decay energy.

[2]The middle row of Fig. 1 shows blank values for nuclei with $84 < Z < 90$ because there is no calculation of fission barriers in this region using the HFB14 model. In the set of reaction rates derived by the Brussels group [44], the fission rates for nuclei with $Z < 90$ has been obtained from ETFSI calculations [58] (see Ref. [59] for more details).
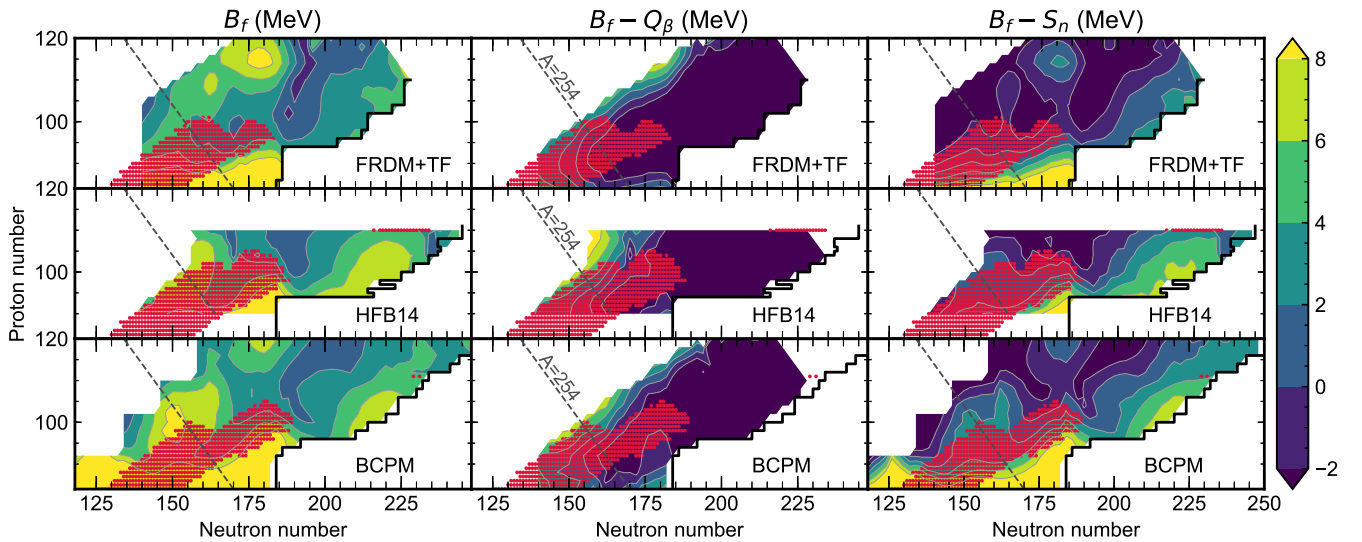
FIG. 1. Highest fission barrier (B_f), and energy windows for β-delayed fission ($B_f - Q_\beta$) and neutron-induced fission ($B_f - S_n$) predicted by FRDM+TF (top panels), HFB14 (middle panels), and BCPM (bottom panels) as a function of proton and neutron number. B_f and S_n values correspond to the nucleus with Z protons and N neutrons, while Q_β values correspond to the FRDM prediction for the $(Z-1, N+1)$ parental nucleus. All the quantities are in MeV. Red circles indicate the *r*-process nuclei produced at $t \approx 10$ s in the hot dynamical ejecta nucleosynthesis.

between the neutron-capture rates and the reverse photodissociation rates is only achieved for the former, but not the latter. The trajectory labeled disk is parametrized following Ref. [48], with an early-time expansion timescale $\tau = 10$ ms, initial entropy $s = 10$ k_B per nucleon, and initial $Y_e = 0.15$. This trajectory mimics the neutron-rich condition found in viscous outflows from postmerger accretion disks [49–53].

Figure 3 shows the *r*-process abundances predicted by FRDM+TF, HFB14, and BCPM models at the time of 1 Gyr for these three different ejecta conditions. All the abundances reproduce the main features of the strong *r*-process pattern, where elements from the second peak up to actinides have been synthesized. Nevertheless, substantial differences between the predicted abundances are observed that will be discussed in the next section.

III. RESULTS

In order to gain insight into the origin of the differences in abundances shown in Fig. 3, we show in Fig. 4 the *r*-process abundances of nuclei beyond $A = 180$ predicted by FRDM+TF, HFB14, and BCPM in each scenario at four different stages of the evolution: at freeze-out, defined as the moment when the neutron-to-seed ratio $n/s = 1$ (where seed includes all nuclei heavier than ^{4}He); at the moment when the average timescale for neutron captures $\tau_{(n,\gamma)}$ equals the average timescale for β decays τ_β; at 1 d, which is taken as a timescale indicative for kilonova observations; and the final abundances calculated at 1 Gyr. For convenience we group this four time steps in three different stages characterizing the evolution of the *r*-process nucleosynthesis.

(i) The neutron-capture phase, which begins when the material becomes gravitationally unbound and lasts until the freeze-out. During this phase, the heaviest

region of the nuclear chart is reached by successive neutron captures and β decays.

(ii) The freeze-out phase, which spans the first seconds after the freeze-out and during which the average timescale for neutron captures $\tau_{(n,\gamma)}$ becomes smaller than the average timescale for β decays τ_β.

(iii) The post-freeze-out phase, when the material starts to decay towards the valley of stability and the abundances pattern is shaped to its final distribution shown in Fig. 3.

The impact of fission on the *r*-process nucleosynthesis varies during these three phases but it mostly manifests through two effects: A direct one, related to the change in the abundances due to the fission rates and yields; and an indirect one, induced by the neutron emission of fission fragments (and the subsequent neutron captures). In the following sections, we will discuss how these effects impact the *r*-process abundances, the evolution of free neutron densities and the rate of energy production at timescales that are relevant for kilonova observations.

A. Impact of fission during the *r* process

We start by determining the mass region in the nuclear chart that is sensitive to the variations in the physics input described in Sec. II. At the freeze-out we find that the contribution of $Z \geqslant 84$ elements in the hot and accretion scenario is negligible for nuclei with $A \leqslant 230$ and constitutes more than 95% of the $A \geqslant 252$ abundances. In the cold scenario these ranges reduce to $A \leqslant 225$ and $A \geqslant 246$. The left column of Fig. 4 shows that the abundances predicted by the three sets of reaction rates are visibly different at the freeze-out. In particular, FRDM+TF exhibits a peak at $A \approx 260$, which
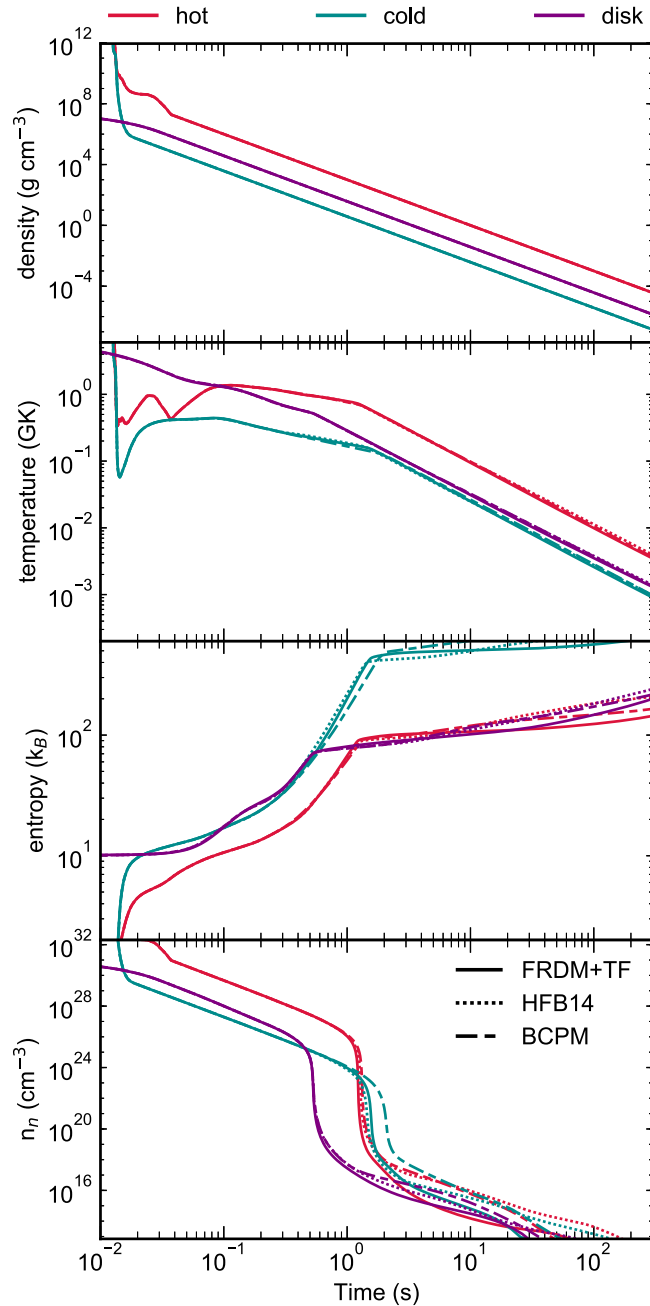
FIG. 2. Evolution of the different thermodynamic variables (from top to bottom): mass density, temperature, entropy, and free neutron number density n_n. The different curves represent the predictions obtained with BCPM (dashed lines), HFB14 (dotted lines), and FRDM+TF (solid lines) for three different trajectories: dynamical hot (red curves), dynamical cold (blue curves), and accretion disk (purple curves) (see text for details).
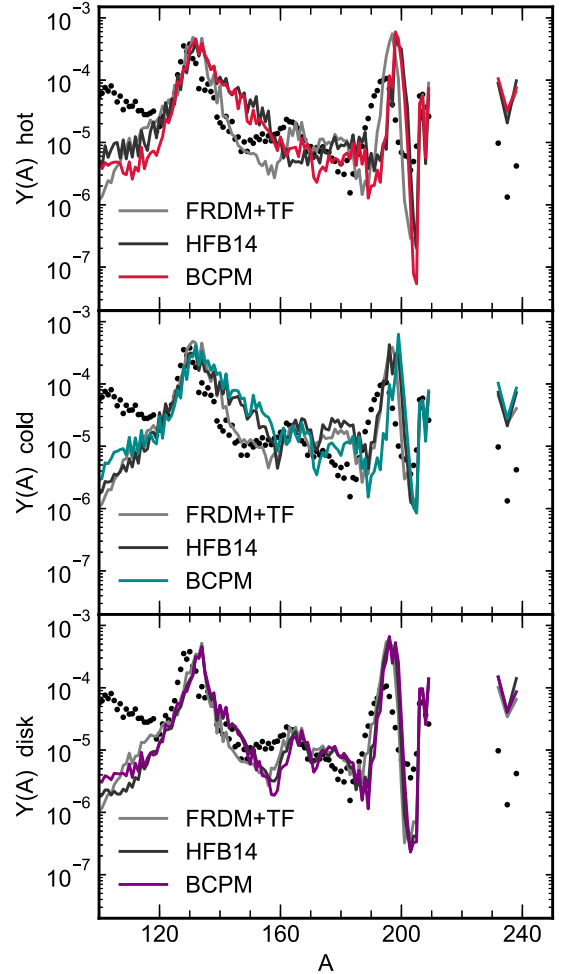

FIG. 3. Abundances as functions of mass number predicted by BCPM, HFB14, and FRDM+TF at 1 Gyr for the three different ejecta conditions: dynamical hot (top panel), dynamical cold (middle panel), and accretion disk (bottom panel). As a reference, black dots show the renormalized solar *r*-process abundances.

is mostly absent in BCPM and HFB14, while both mean-field models predict a large accumulation of material around $A \gtrsim 280$. By comparing the nuclear properties of the three models, we found that two main factors determine these variations. First, jumps in the neutron separation energies (and, consequently, in shell gap energies) can entail accumulation of material at different mass numbers, particularly during this

initial stage of the evolution when neutron-captures dominate over β decays. Second, changes in the fission barriers modify the survival probability of nuclei and determine the end of the *r*-process path. In the case of the abundances plotted in Fig. 4, FRDM predicts a strong shell gap at $N = 172$, which results in the abundances peak at $A \approx 260$. Conversely, the larger fission barriers and shell gap predicted by HFB14 and BCPM at $N = 184$ [38] are responsible for the larger accumulation of material at $A \approx 280$. These variations are also visible in Fig. 5, where the *r*-process path at freeze-out predicted by BCPM, HFB14, and FRDM+TF for the hot dynamical trajectory is depicted. At $N = 184$, the *r*-process path obtained with BCPM and HFB14 models can substantially populate nuclei up to $^{280}_{96}$Cm ($t_{1/2} = 84$ ms, according to the β-decay half-life predictions of Ref. [39]), while the FRDM+TF *r*-process path accumulates material mostly around $^{278}_{94}$Pu ($t_{1/2} = 32$ ms). We recall that around freeze-out the abundances are to a very good approximation proportional to the β-decay lifetimes (see, e.g., Ref. [54]).
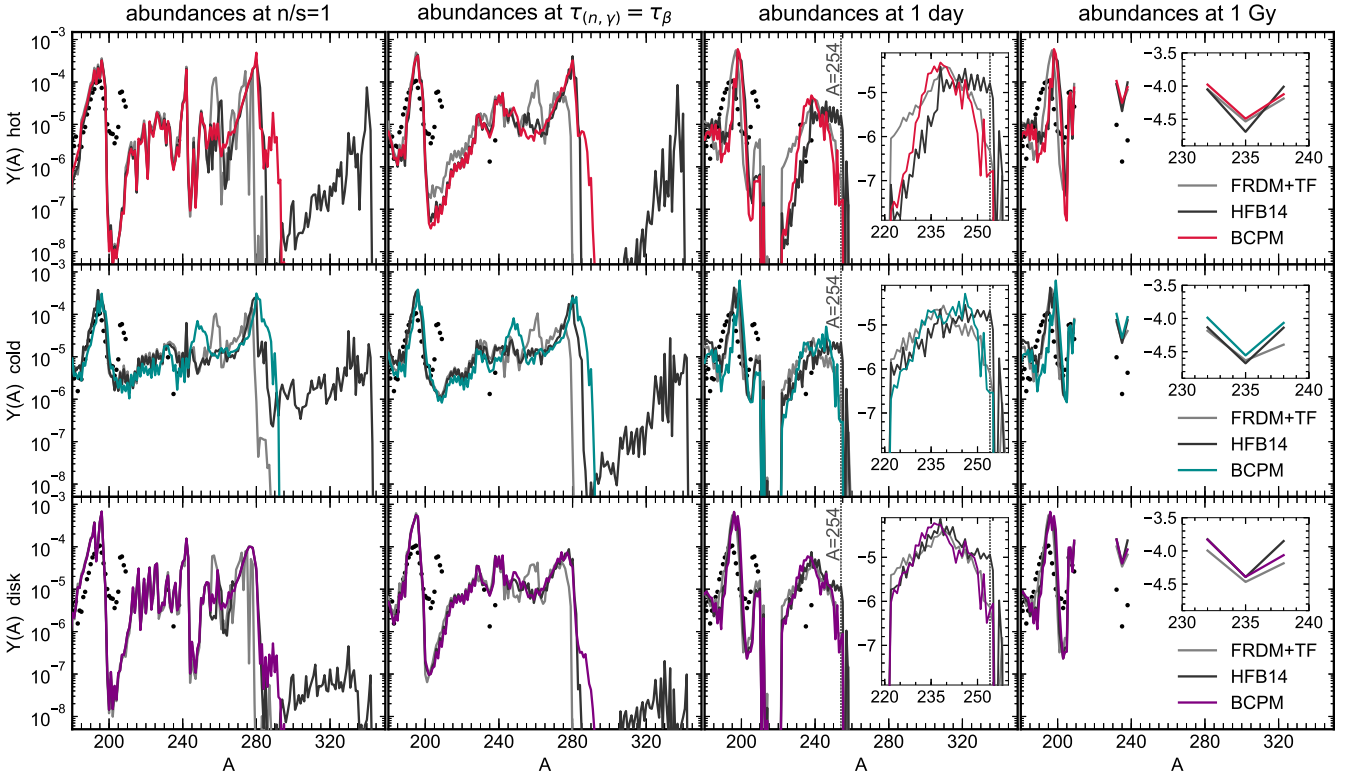
FIG. 4. Abundances as functions of mass number predicted by FRDM+TF, HFB14, and BCPM at four different times. Each row represent a different type of ejecta: dynamical hot (top panels), dynamical cold (middle panels), and accretion disk (bottom panels). Insets show the abundances prediction in $\log_{10}$ scale for particular mass regions. At $t = 1$ day, mass number $A = 254$ is marked with a gray vertical dotted line. Black dots represent solar *r*-process abundances, which are renormalized by the same factor in all plots.

Figure 4 also shows that the accumulation of nuclei with $A \gtrsim 260$ vary with the astrophysical scenario. We find that in the accretion trajectory the total abundance of fissioning nuclei is a factor two smaller than the dynamical scenarios and that no fission cycles occur during the *r* process. This is because the conditions in this trajectory are less neutron rich than in the dynamical ones: namely, the initial neutron-to-seed ratio is $n/s \approx 120$, compared to $n/s \approx 600$ and $n/s \approx 1200$ of the hot and cold dynamical ejecta, respectively. These conditions do not allow the *r* process to efficiently overcome the $N = 184$ shell closure, since the number of free neutrons is mostly depleted when the material reaches the $A \approx 280$ region.

B. Impact of fission at the freeze-out

The bottom panel of Fig. 2 shows that the choice of the reaction rates substantially change the evolution of n_n after the freeze-out. In order to understand the origin of such differences, we study the contribution of individual reaction channels to the change of the neutron abundance $Y_n = n_n m_u / \rho$, where m_u is the atomic mass unit and ρ is the mass density. We notice that after the freeze-out and until $\approx 10^3$ seconds, the total dY_n/dt is much smaller than the dY_n/dt contribution from single channels, with the exception of (γ, n), which quickly becomes negligible. This suggests that free neutrons are in a condition of quasiequilibrium for

an extended period of time:

$$\frac{dY_n}{dt} = \frac{dY_n}{dt}\bigg|_{\text{prod}} - \frac{dY_n}{dt}\bigg|_{\text{abs}} \approx 0, \tag{1}$$

during which nuclei efficiently absorb and release neutrons. Considering a network formed by neutron captures, photodissociations, β decays, and neutron-induced/β-delayed/spontaneous fission, one gets that the evolution of Y_n can be written as:

$$\frac{dY_n}{dt} = Y_s \bigg\{ \bar{\lambda}_{(\gamma, n)} + \bar{\nu}_\beta \bar{\lambda}_\beta + \bar{\nu}_{\beta\text{fis}} \bar{\lambda}_{\beta\text{fis}} + \bar{\nu}_{\text{sf}} \bar{\lambda}_{\text{sf}}$$

$$- Y_n \frac{\rho}{m_u} [(1 - \bar{\nu}_{(n,\text{fis})}) \overline{\langle \sigma v \rangle}_{(n,\text{fis})} + \overline{\langle \sigma v \rangle}_{(n,\gamma)}] \bigg\} \tag{2}$$

$$\approx 0,$$

where $\bar{\nu}_i$ is the neutron multiplicity of the channel i that releases neutrons, λ_i the channel rate and $\langle \sigma v \rangle_i$ the cross section averaged over a Maxwell-Boltzmann energy distribution. The bar over the different quantities denotes average over the composition of seed nuclei, $Y_s = \sum_j Y_j$.

$$\bar{\lambda}_i = \frac{\sum_j \lambda_i(j) Y_j}{\sum_j Y_j}, \quad \bar{\nu}_i = \frac{\sum_{j,k} k \lambda_{i,k}(j) Y_j}{\sum_{j,k} \lambda_{i,k}(j) Y_j}, \tag{3}$$

with $\lambda_{i,k}(j)$ the rate for nucleus j to produce k neutrons via the reaction channel i and $\lambda_i(j) = \sum_k \lambda_{i,k}(j)$. Equation (2)
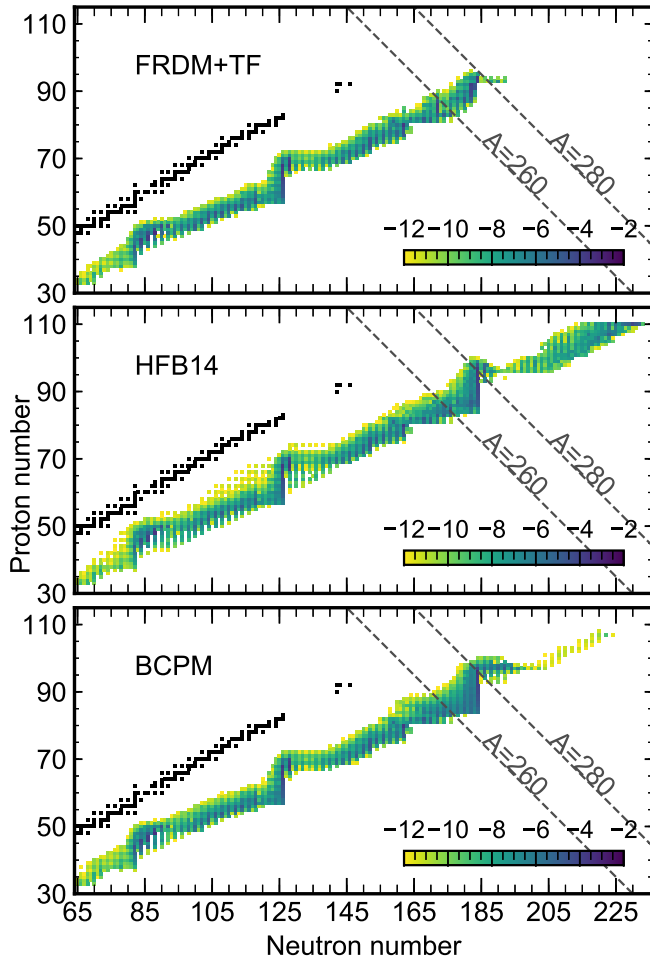
FIG. 5. Abundances (in $\log_{10}$ scale) at freeze-out predicted by FRDM+TF (top panel), HFB14 (middle plot), and BCPM (bottom plot) in the hot dynamical ejecta. Black squares represent stable nuclei.
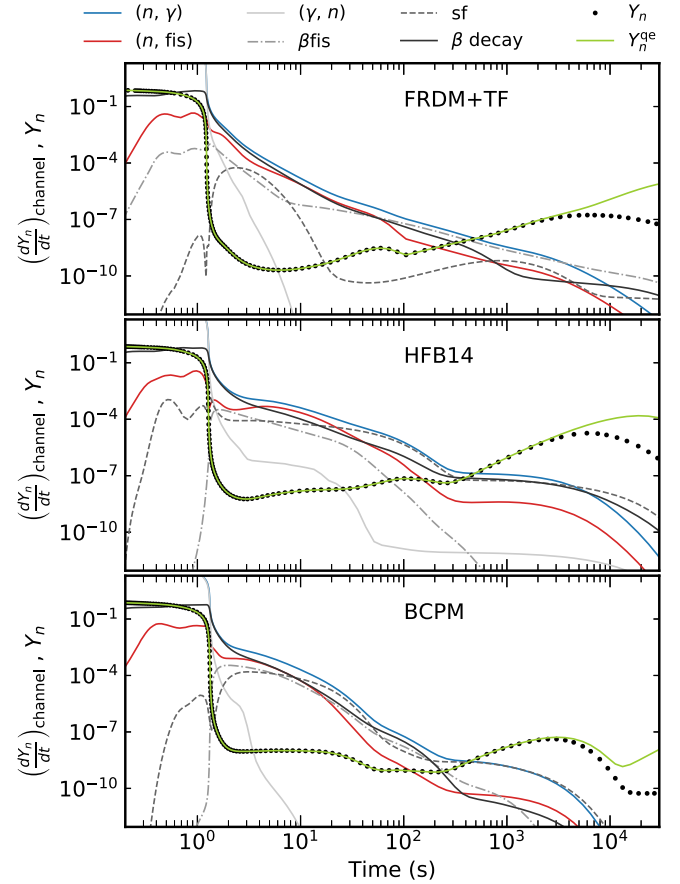

FIG. 6. Contribution of single channels in Eq. (2) to dY_n/dt obtained with different reaction rates in the hot dynamical scenario. The exact neutron abundance Y_n (black circles) are compared with those predicted by Eq. (4) assuming quasiequilibrium (green line).

allows us to estimate Y_n given the seed-averaged decay rates:

$$Y_n \approx \frac{\bar{\lambda}_{(\gamma,n)} + \bar{\nu}_\beta \bar{\lambda}_\beta + \bar{\nu}_{\beta\mathrm{fis}} \bar{\lambda}_{\beta\mathrm{fis}} + \bar{\nu}_{\mathrm{sf}} \bar{\lambda}_{\mathrm{sf}}}{\langle\sigma v\rangle_{(n,\gamma)} + (1 - \bar{\nu}_{(n,\mathrm{fis})})\langle\sigma v\rangle_{(n,\mathrm{fis})}} \frac{m_u}{\rho}, \quad (4)$$

which shows that Y_n is directly proportional to the rates producing neutrons and inversely proportional to the difference between production and absorption rates involving neutrons as reactants. This implies that β decay, β-delayed fission, and spontaneous fission contribute differently to Y_n than neutron-induced fission, and that small variations in fission rates can substantially modify the evolution of neutron abundances if fission is a relevant source of neutrons.

To better assess the impact of different decay channels on Y_n, Fig. 6 shows the individual contributions to dY_n/dt of Eq. (4) predicted by different set of reaction rates in the hot scenario. In this plot one can notice that at 10 s the Y_n obtained with FRDM+TF is more than one order of magnitude smaller than in the HFB14 and BCPM cases. This is because of the larger $\overline{\langle\sigma v\rangle}_{(n,\gamma)}$ predicted within FRDM+TF, which increases the denominator in Eq. (4), while the accumulation

of fissioning nuclei in BCPM and HFB14 enhances the numerator by boosting the contribution from both fission and β-delayed neutron emission. In Secs. III D and III E we will discuss how this increase of the free neutron abundances (and, consequently, of the free neutron number densities) plays an important role in the production and destruction of nuclei relevant for kilonova observation.

C. Impact of fission on final abundances

Figure 3 shows that the changes in the reaction rates of nuclei with $Z \geqslant 84$ in the dynamical scenarios produce large variations in the final abundances above the second peak ($A \gtrsim 140$) and in the location of the third peak ($A \approx 195$). The former are directly populated by the fission fragments of nuclei around $A = 280$, which is a region that the *r*-process path can efficiently reach in the case of large fission barriers around $N = 184$ (HFB14 and BCPM) within the neutron-rich conditions found in the dynamical scenarios (see discussion in Sec. III A). As already explored in different studies [23,24,31–33,55], the final shape in this mass region strongly depends on the theoretical fission yields assumed for such neutron-rich
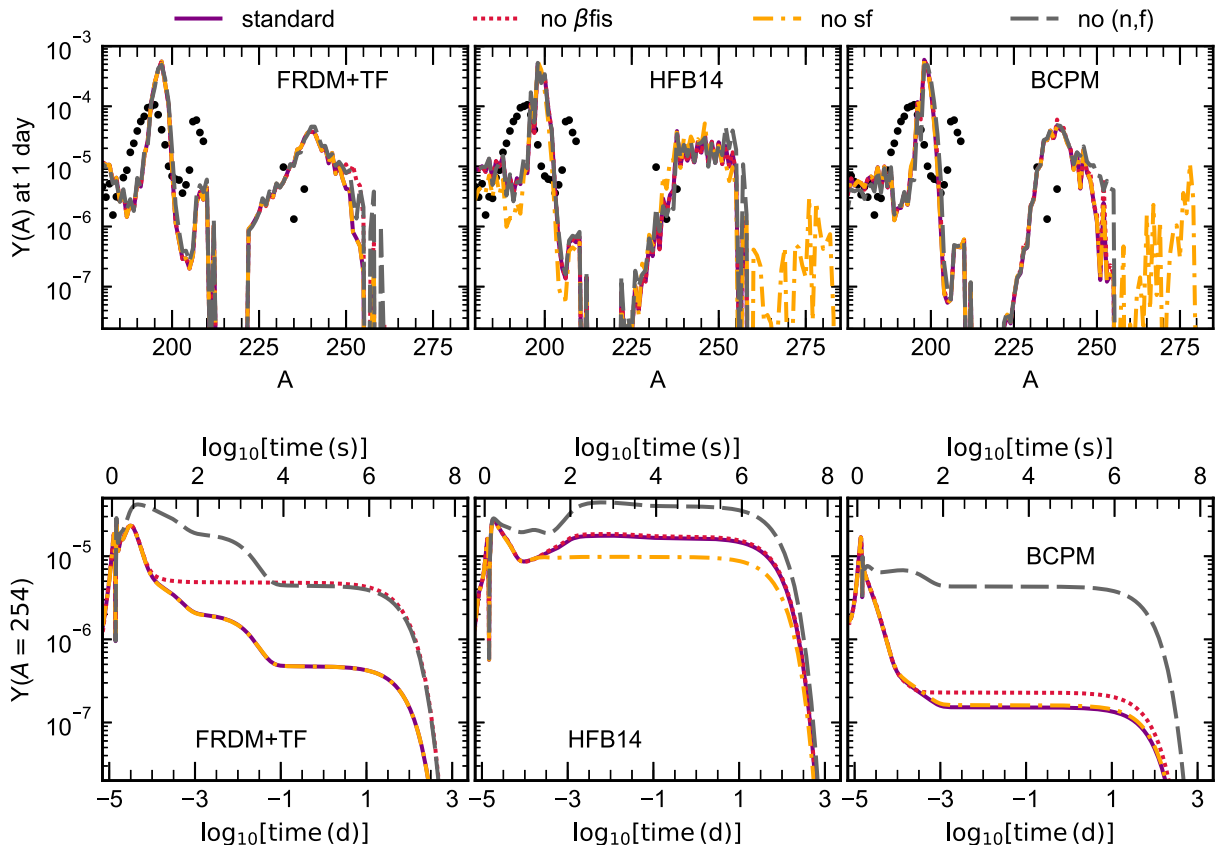
FIG. 7. Impact of single fission channels on the abundances of nuclei with $A \gtrsim 250$ at 1 d (top panels) and on the evolution of $A = 254$ abundances (bottom panels) for the hot dynamical ejecta. The different curves show the abundances predicted when different fission channels are suppressed: β-delayed fission (βfis, red dashed line), spontaneous fission (*sf*, yellow dashed line) and neutron-induced fission ((n, f), gray dashed line). The purple solid line corresponds to standard calculations, when all the fission are included. Left, middle, and right panels correspond to FRDM+TF, HFB14, and BCPM, respectively.

nuclei (see Ref. [20] regarding the fission fragments distri-butions used in this work). Conversely, the position of the third peak is determined by the interplay between β-decay rates and late neutron captures during the freeze-out [33]. Figure 3 shows that the largest shifts are obtained with HFB14 and BCPM in the hot dynamical scenario, where the fission of $A = 280$ nuclei increases n_n through neutron emission as discussed in Sec. III B. Figure 3 also shows that in the case of the accretion disk all the models predict a very similar final abundance patterns, mainly because in this case fission con-tributes very little to the final abundance that are determined mostly by the masses and β decays of nuclei with $Z < 84$ that remain unchanged in all the calculations.

Finally, we notice that in all the calculations the abun-dances of nuclei in the lead peak ($A \approx 208$) and those of the uranium and thorium cosmochronometers are also very similar (see insets at $t = 1$ Gyr in Fig. 4). This result in-dicates that the progenitors of these nuclei have the same nuclear properties, which is consistent with our discussion in Sec. III A where we argued that modifying the nuclear prop-erties of elements with $Z \geqslant 84$ only captures the sensitivity of nuclei with $A \gtrsim 252$. It is therefore possible to conclude that most the material with $Z \geqslant 84$ created during the *r*-process nucleosynthesis fissions.

D. Fission and the destruction of $A \gtrsim 250$ nuclei

One feature shown in Fig. 4 is that, at the time of a day, BCPM and FRDM+TF predict a drastic drop of the abun-dances for nuclei with $A \gtrsim 250$, while in HFB14 calculation this dip is displaced to $A \gtrsim 255$. These differences have im-portant consequences in terms of kilonova observation, since the decay by spontaneous fission of ^{254}Cf, $t_{1/2} = 60.5 \pm 0.2$ d [56], can sensibly impact the shape and magnitude of the kilonova light curves at $t \gtrsim 100$ days [17,18]. Therefore, it is important to understand the mechanisms that are responsible for the destruction of these nuclei as they also determine the amount of ^{254}Cf that survives at kilonova times. For this pur-pose, we performed additional calculations by switching off different fission channels (neutron-induced, β-delayed, and spontaneous fission) and compare the impact of each channel on the remaining abundance of $A \gtrsim 250$ nuclei at 1 d. While we only discuss below the results obtained in the hot dynam-ical case, we note that similar outcomes are obtained in the cold and accretion disk scenarios.

The upper panels in Fig. 7 show the abundances predicted with FRDM+TF (left panel) HFB14 (middle panel), and BCPM (right panel) when different fission channels are turned off. Spontaneous and β-delayed fission are suppressed from
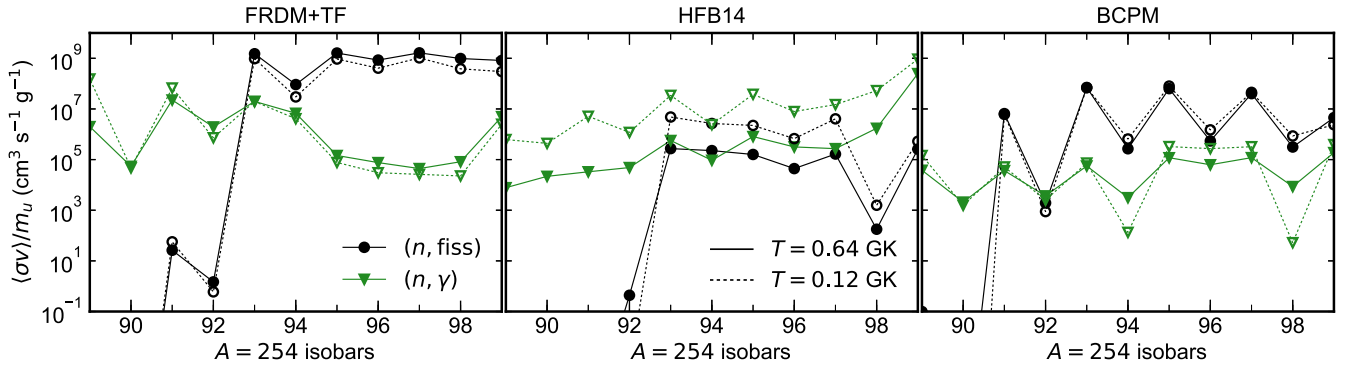
FIG. 8. Neutron-induced fission (black circles) and neutron capture (green triangles) stellar reaction rates predicted at $T = 0.64$ GK (solid lines, solid symbols) and $T = 0, 12$ GK (dotted lines, hollow symbols) by FRDM+TF (left panel), HFB14 (middle panel), and BCPM (right panel).

the beginning of the simulation, while neutron-induced fission was turned off only after the freeze-out. We point out that only theoretical rates have been switched off. We find that within each set of reaction rates the abundances drop for the same value of A, indicating that the drop is a generic feature of the behavior of fission barriers in the region. This is confirmed by comparing the abundance distribution after the r-process freeze-out to the fission barriers shown in Fig. 1. Nuclei that are present at $t \approx 10$ s in the hot dynamical ejecta scenario are plotted as solid symbols. Left panels show that the abundance distributions closely follows contour lines of constant fission barrier height, and that none of the models predict the synthesis of nuclei with $B_f < 2$ MeV. We conclude therefore that the destruction mechanism is related to the presence of low fission barriers, which in turn make those nuclei unstable against fission regardless of the astrophysical environment. For BCPM and FRDM+TF such region inhibits the survival of nuclei with $A > 250$, while the larger fission barriers predicted by HFB14 allow nuclei up to $A = 255$ to remain. The only calculations where nuclei with $A > 255$ survive at 1 d are for the BCPM and HFB14 rates without spontaneous fission. In both cases, the larger $B_f - Q_\beta$ predicted by these two models around $N = 184$ allow part of the material to undergo multiple β decays before entering in the region of low B_f and fission. One should notice that in Fig. 1 there are nuclei with negative energy window for β-delayed fission ($B_f - Q_\beta$) that are populated. The reason for this is twofold: first, the β-decay proceeds mainly via states with low excitation energy, hence it is the magnitude of the barrier and not necessarily $B_f - Q_\beta$ that determines the fission survival probability after β decay. Second, nuclei populated in Fig. 1 have $S_n < B_f$, as evinced by the right panels in the same plot, which favors the (n, γ) reaction over $(n, \text{fission})$.

Bottom panels in Fig. 7 show the total $A = 254$ abundance predicted in the hot dynamical ejecta by the different sets of reaction rates. From this plot it is possible to conclude that in all the models neutron-induced fission is the main mechanism responsible for the destruction of $A = 254$ isobars, but the impact of this channel strongly depends on the adopted nuclear input. There are mainly two reasons causing such variations: The first one is related to the ratio between neutron captures and neutron-induced fission, which determine the

survival probability of the nucleus after capturing a neutron. Figure 8 shows the neutron capture and neutron-induced fission reaction rates for different $A = 254$ isobars predicted by the three nuclear models at 0.64 GK and 0.12 GK, which are the temperatures at freeze-out for the hot and dynamical trajectory, respectively. In the case of BCPM (FRDM+TF), neutron-induced fission dominates over neutron captures for nuclei above $^{254}_{91}\text{Pa}_{163}$ ($^{254}_{93}\text{Np}_{161}$), suggesting a more efficient destruction of ^{254}Cf progenitors compared to HFB14, for which neutron-induced fission is mostly subdominant along the isobars. The second aspect are variations in the neutron number density (n_n), which regulate the competition between neutron-induced fission and other decay channels such as β-decay rates. As discussed in Sec. III B, after the freeze-out BCPM and HFB14 predict larger n_n than FRDM+TF because of the larger amount of fissioning nuclei emitting neutrons, which in turn boosts the destruction of $A = 254$ isobars in BCPM due to the dominance of neutron-induced fission over neutron capture showed in Fig. 8. This feature is reminiscent of the self-sustained mechanism occurring in nuclear reactors, where the free neutrons released after the freeze-out generate new neutron-induced fission events. We conclude that the destruction of $A = 254$ isobars should be considered as a more general feature, where the destruction rate of nuclei post-freeze-out is strongly related to variations in the neutron number density since this directly determines the neutron captures and neutron-induced fission rates. On the other hand, Fig. 7 shows that β-delayed fission only operates to destruct the $A = 254$ isobars at later times with FRDM+TF model, since the large $B_f - Q_\beta$ predicted by BCPM and HFB14 disfavor this fission channel (see middle panels in Fig 1). Finally, in Fig. 8 we observe that the competition between reaction rates is not affected by variations in temperature given by the different trajectories explored in this study.

E. Impact of fission on abundance of nuclei with $A = 222$–225

Besides ^{254}Cf, another relevant region for kilonova observations are actinides with mass number $A = 222$–225 [18]. If these α emitters can be produced in a substantial amount, their released energy could dominate the heating rates at timescales
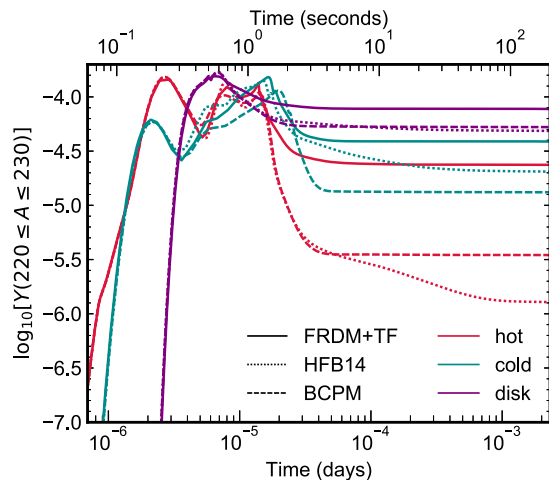
FIG. 9. Evolution of the total $220 \leqslant A \leqslant 230$ abundance predicted by FRDM+TF (solid lines), HFB14 (dotted lines), and BCPM (dashed lines) for different trajectories.

of weeks to months, providing a unique signature of production of heavy nuclei during the *r* process. The insets of Fig. 4 at 1 d show that the abundances of such nuclei depend on the set of stellar reaction rates. Particularly, BCPM and HFB14 models in the dynamical scenarios predict smaller abundance compared to FRDM+TF, as shown in Fig. 9 where the abundance evolution of nuclei with $220 \leqslant A \leqslant 230$ is plotted for the different nuclear models and trajectories. Since $A = 220$–230 abundances are dominated by elements with $Z \leqslant 83$, whose nuclear properties are fully determined by FRDM, we conclude that the variations observed in Fig. 4 and 9 are driven by the changes in free neutron number densities discussed in Sec. III B. This conclusion is consistent with the fact that the depletion observed in Fig. 9 occurs in the first 1–2.5 s after the freeze-out, that is the timescale when fissioning nuclei enhance the neutron abundance. As a consequence, BCPM and HFB14 in the dynamical scenarios show a larger exhaustion compared to FRDM+TF due to the larger accumulation of fissioning material, while all the models predict similar final abundances in the accretion case.

We point out that at 1 d the total abundance of nuclei with $220 \leqslant A \leqslant 260$ is similar in all the calculations, suggesting that the underproduction of α emitters in BCPM and HFB14 calculations is related to a transport of material to heavier masses rather than to a destruction of those nuclei.

F. Heating rates and kilonova light curves

In the previous two sections we analyzed the role of fission in the production of nuclei that may produce signatures relevant to the synthesis of heavy nuclei during the *r* process. In order to properly address the possible implications for late-time kilonova nebular observations, in this section we discuss the impact of our calculations in both the nuclear energy release and the ejecta heating rates. Figure 10 shows the nuclear energy release rate produced by fission, β and α decays as a function of time obtained with FRDM+TF, HFB14, and BCPM models for the different ejecta conditions. The fission heating rates in the range 10–1000 days are dominated by the spontaneous fission decay of ^{254}Cf. Depending on the set of reaction rates, the abundances of this nucleus change substantially and hence its contribution to the nuclear energy release. For both FRDM+TF and BCPM the contribution of ^{254}Cf to the total heating is negligible independently of the astrophysical scenario considered. For HFB14 heating by ^{254}Cf dominates around 100 d. This is due to the fact that for FRDM+TF and BCPM (n, fiss) completely dominates over (n, γ) for nuclei around $A \approx 254$ (see Fig. 8 and discussion in Sec. III D) while for HFB14 (n, γ) and (n, fiss) are of similar magnitude leading to a larger abundance of ^{254}Cf in the three scenarios.

Besides the variations at 10–1000 d, Fig. 10 shows that the models predict different rates also at $t \approx 0.1$ d. Comparing FRDM+TF and BCPM, one can notice that the latter shows a sharp transition, which is mostly absent in the former. We find that in FRDM+TF the contribution to the energy production of fission is mainly sustained by the neutron-induced fission flows (defined as the product of fission rate and nuclear abundance) of ^{241,242,244}Pu. In BCPM, such plutonium isotopes are less abundant and have smaller neutron-induced fission rates resulting in a quench of the radioactive energy emitted by fission. HFB14 predicts a large contribution of fission to
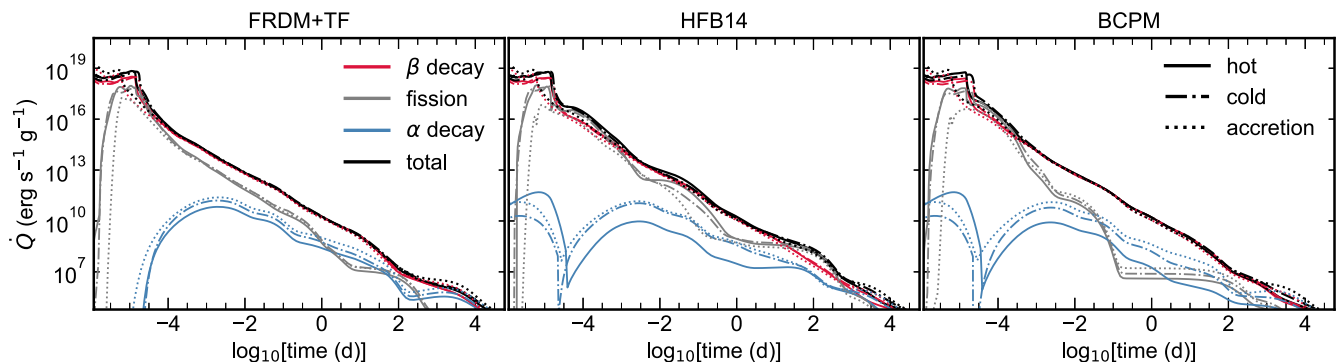

FIG. 10. Radioactive energy emitted by β decay (gray lines), α decay (blue lines), and fission (red lines) as a function of time for different ejecta conditions: dynamical hot (solid lines), dynamical cold (dash-dotted lines), and accretion disk (dotted lines). Top, middle, and bottom panel shows the results predicted by FRDM+TF, HFB14, and BCPM, respectively.
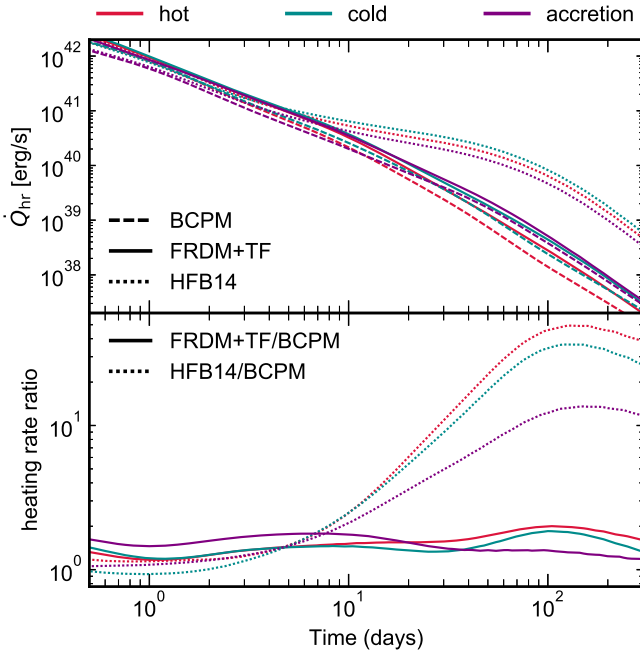
FIG. 11. Top: Ejecta heating rate as a function of time predicted with BCPM (dash lines), HFB14 (dotted lines), and FRDM+TF (solid lines) for different scenarios. Bottom: Evolution of the ratio between ejecta heating rates for different scenarios: FRDM+TF/BCPM (solid lines) and HFB14/BCPM (dotted lines).

the energy production at timescales of 0.1 d that can even dominate over β decay. This may be an artifact caused by the accumulation of nuclei with $Z = 110$ at the edge of our nuclear network (see middle panels in Fig. 1) and will require further calculations with an extended network.

In addition to the heating from fission and the role of spontaneous fission of ^{254}Cf, Fig. 10 shows also the contribution of α decay powered by the decay chains of nuclei with $222 \leqslant A \leqslant 225$ during the relevant kilonova timescale of 3–100 d [18]. We find that for all models and astrophysical scenarios the contribution of α decay is subdominant. We will recall, however, that the method followed in this work does not fully capture the nuclear sensitivity of this mass region, since the progenitors of $222 \leqslant A \leqslant 225$ are elements with $Z \leqslant 83$. Therefore in order to better asses the uncertainty in the production of these α emitters, additional sensitivity studies including variations in the nuclear properties of lighter elements are in order.

Finally, Fig. 11 shows the time evolution of the ejecta heating rate $\dot{Q}_{hr}$, which mimics the bolometric luminosity of the kilonova at $t \gtrsim$ days post the light-curve peak. Calculations were performed as described in Ref. [18], which include thermalization corrections, assuming an ejecta mass $M_{ej} = 0.04 \, M_\odot$ with an expanding velocity $v_{ej} = 0.1 \, c$. The impact of the ^{254}Cf is clearly noticeable at $t \approx 100$ d, where the predictions obtained with FRDM+TF, HFB14, and BCPM visibly differ. In the dynamical scenarios, the smaller amount of ^{254}Cf predicted with BCPM [$Y(^{254}$Cf$) \approx 1.5 \times 10^{-7}$] results in a heating rate 50 times smaller than the one predicted with HFB14 [$Y(^{254}$Cf$) \approx 1.6 \times 10^{-5}$] and two times smaller

than the one obtained with the FRDM+TF rates [$Y(^{254}$Cf$) \approx 4.7 \times 10^{-7}$]. One shall notice that changes in ^{254}Cf abundances and ejecta heating rates are not proportional due to the β-decay contribution to the heating rate. Nevertheless, this result confirms the high sensitivity of kilonova light curve to the amount of ^{254}Cf fissioning at timescales relevant for astronomical observations [17,18], which translates into a large uncertainty in the heating rates due to variations in the fission properties of translead nuclei. We also notice that despite the abundances of nuclei with $135 \lesssim A \lesssim 200$ are largely affected by the direct impact of fission, the β-decay heating rate at earlier times are only affected by $\lesssim 50\%$.

IV. CONCLUSIONS

We explored the impact of fission on the *r*-process nucleosynthesis yields in neutron star mergers and the associated nuclear energy release rates relevant for kilonovae. We used three different sets of stellar reaction rates, one of which was recently developed using consistent nuclear energy density functional calculations of nuclear masses, fission barriers, and collective inertias [38]. Our calculations show that for the most neutron-rich conditions, like those found in the dynamical ejecta, the stability against fission of nuclei around the neutron shell closure $N = 184$ is crucial for the buildup of fissioning material during the *r* process. The fission of these material after the *r*-process freeze-out can release a large amount of neutrons and significantly alter the free neutrons number density of the ejecta around $1 \, \text{s} \lesssim t \lesssim 10 \, \text{s}$. Consequently, the neutron-induced fission and neutron captures associated with these free neutrons can have strong impact on the abundances of nuclei in the mass number region $A = 220$–260, including the α-decaying nuclei with $222 \leqslant A \leqslant 225$ and the ^{254}Cf fission, affecting the ejecta heating rates on timescales relevant for kilonova light-curve predictions.

In conclusion, we find a connection between the amount of material produced around $A = 280$ at early stages of the evolution and the amount of ^{254}Cf produced at timescales relevant for kilonova observation. This result suggests that future detection or nondetection of ^{254}Cf on kilonova light curves may help to constraint the yields of nuclei around $A \approx 280$ and learn about the nuclear properties in a region that in the foreseeable future will not be experimentally accessed [57].

[1] E. M. Burbidge, G. R. Burbidge, W. A. Fowler, and F. Hoyle, Rev. Mod. Phys **29**, 547 (1957).

[2] A. G. W. Cameron, Publ. Astron. Soc. Pac. **69**, 201 (1957).

[3] LIGO Scientific Collaboration and Virgo Collaboration, B. P. Abbott *et al.*, Phys. Rev. Lett. **119**, 161101 (2017).

[4] B. P. Abbott *et al.*, Astrophys. J. **848**, L12 (2017).

[5] J. M. Lattimer and D. N. Schramm, Astrophys. J. **192**, L145 (1974).

[6] J. M. Lattimer and D. N. Schramm, Astrophys. J. **210**, 549 (1976).

[7] E. Symbalisty and D. N. Schramm, Astrophys. Lett. **22**, 143 (1982).

[8] C. Freiburghaus, S. Rosswog, and F.-K. Thielemann, Astrophys. J. **525**, L121 (1999).

[9] L.-X. Li and B. Paczyński, Astrophys. J. **507**, L59 (1998).

[10] B. D. Metzger, G. Martínez-Pinedo, S. Darbha, E. Quataert, A. Arcones, D. Kasen, R. Thomas, P. Nugent, I. V. Panov, and N. T. Zinner, Mon. Not. Roy. Astron. Soc. **406**, 2650 (2010).

[11] L. F. Roberts, D. Kasen, W. H. Lee, and E. Ramirez-Ruiz, Astrophys. J. **736**, L21 (2011).

[12] S. Goriely, S. Hilaire, A. J. Koning, and R. Capote, J. Korean Phys. Soc. **59**, 979 (2011).

[13] J. J. Cowan, C. Sneden, J. E. Lawler, A. Aprahamian, M. Wiescher, K. Langanke, G. Martínez-Pinedo, and F.-K. Thielemann, arXiv:1901.01410 [Rev. Mod. Phys. (to be published)].

[14] D. Watson, C. J. Hansen, J. Selsing, A. Koch, D. B. Malesani, A. C. Andersen, J. P. U. Fynbo, A. Arcones, A. Bauswein, S. Covino, A. Grado, K. E. Heintz, L. Hunt, C. Kouveliotou, G. Leloudas, A. J. Levan, P. Mazzali, and E. Pian, Nature (London) **574**, 497 (2019).

[15] D. Kasen, B. D. Metzger, J. Barnes, E. Quataert, and E. Ramirez-Ruiz, Nature (London) **551**, 80 (2017).

[16] K. Kawaguchi, M. Shibata, and M. Tanaka, Astrophys. J. **865**, L21 (2018).

[17] Y.-L. Zhu, R. T. Wollaeger, N. Vassh, R. Surman, T. M. Sprouse, M. R. Mumpower, P. Möller, G. C. McLaughlin, O. Korobkin, T. Kawano, P. J. Jaffke, E. M. Holmbeck, C. L. Fryer, W. P. Even, A. J. Couture, and J. Barnes, Astrophys. J. **863**, L23 (2018).

[18] M.-R. Wu, J. Barnes, G. Martínez-Pinedo, and B. D. Metzger, Phys. Rev. Lett. **122**, 062701 (2019).

[19] M. M. Kasliwal, D. Kasen, R. M. Lau, D. A. Perley, S. Rosswog, E. O. Ofek, K. Hotokezaka, R.-R. Chary, J. Sollerman, A. Goobar, and D. L. Kaplan, Mon. Not. Roy. Astron. Soc. Letters slz007 (2019), doi: 10.1093/mnrasl/slz007.

[20] J. J. Mendoza-Temis, M.-R. Wu, K. Langanke, G. Martínez-Pinedo, A. Bauswein, and H.-T. Janka, Phys. Rev. C **92**, 055805 (2015).

[21] J. Barnes, D. Kasen, M.-R. Wu, and G. Martínez-Pinedo, Astrophys. J. **829**, 110 (2016).

[22] S. Rosswog, U. Feindt, O. Korobkin, M.-R. Wu, J. Sollerman, A. Goobar, and G. Martínez-Pinedo, Class. Quantum Gravity **34**, 104001 (2017).

[23] N. Vassh, R. Vogt, R. Surman, J. Randrup, T. M. Sprouse, M. R. Mumpower, P. Jaffke, D. Shaw, E. M. Holmbeck, Y.-L. Zhu, and G. C. McLaughlin, J. Phys. G: Nucl. Part. Phys. **46**, 065202 (2019).

[24] N. Vassh, M. R. Mumpower, G. C. McLaughlin, T. M. Sprouse, and R. Surman, Astrophys. J. **896**, 28 (2020).

[25] F.-K. Thielemann, J. Metzinger, and H. V. Klapdor, Z. Phys. A **309**, 301 (1983).

[26] I. V. Panov and F.-K. Thielemann, Astron. Lett. **30**, 647 (2004).

[27] I. V. Panov, I. Y. Korneev, and F. K. Thielemann, Astron. Lett. **34**, 189 (2008).

[28] I. Petermann, K. Langanke, G. Martínez-Pinedo, I. V. Panov, P.-G. Reinhard, and F.-K. Thielemann, Eur. Phys. J. A **48**, 122 (2012).

[29] O. Korobkin, S. Rosswog, A. Arcones, and C. Winteler, Mon. Not. Roy. Astron. Soc. **426**, 1940 (2012).

[30] I. V. Panov, I. Y. Korneev, G. Martínez-Pinedo, and F.-K. Thielemann, Astron. Lett. **39**, 150 (2013).

[31] S. Goriely, Eur. Phys. J. A **51**, 22 (2015).

[32] S. Goriely and G. Martínez-Pinedo, Nucl. Phys. A **944**, 158 (2015).

[33] M. Eichler, A. Arcones, A. Kelić-Heil, O. Korobkin, K. Langanke, T. Marketin, G. Martínez-Pinedo, I. V. Panov, T. Rauscher, S. Rosswog, C. Winteler, N. T. Zinner, and F.-K. Thielemann, Astrophys. J. **808**, 30 (2015).

[34] M. R. Mumpower, T. Kawano, T. M. Sprouse, N. Vassh, E. M. Holmbeck, R. Surman, and P. Möller, Astrophys. J. **869**, 14 (2018).

[35] E. M. Holmbeck, T. M. Sprouse, M. R. Mumpower, N. Vassh, R. Surman, T. C. Beers, and T. Kawano, Astrophys. J. **870**, 23 (2018).

[36] M. Baldo, L. M. Robledo, P. Schuck, and X. Viñas, Phys. Rev. C **87**, 064305 (2013).

[37] S. A. Giuliani and L. M. Robledo, Phys. Rev. C **88**, 054325 (2013).

[38] S. A. Giuliani, G. Martínez-Pinedo, and L. M. Robledo, Phys. Rev. C **97**, 034323 (2018).

[39] P. Möller, B. Pfeiffer, and K.-L. Kratz, Phys. Rev. C **67**, 055802 (2003).

[40] T. Rauscher and F.-K. Thielemann, At. Data. Nucl. Data Tables **75**, 1 (2000).

[41] I. V. Panov, I. Y. Korneev, T. Rauscher, G. Martínez-Pinedo, A. Kelić-Heil, N. T. Zinner, and F.-K. Thielemann, Astron. Astrophys. **513**, A61 (2010).

[42] P. Möller, J. R. Nix, W. D. Myers, and W. J. Świątecki, At. Data. Nucl. Data Tables **59**, 185 (1995).

[43] W. D. Myers and W. J. Świątecki, Phys. Rev. C **60**, 014606 (1999).

[44] Y. Xu, S. Goriely, A. Jorissen, G. L. Chen, and M. Arnould, Astron. Astrophys. **549**, A106 (2013).

[45] S. Goriely, N. Chamel, and J. M. Pearson, Phys. Rev. C **88**, 024308 (2013).

[46] S. Goriely, S. Hilaire, A. J. Koning, M. Sin, and R. Capote, Phys. Rev. C **79**, 024612 (2009).

[47] A. Bauswein, S. Goriely, and H.-T. Janka, Astrophys. J. **773**, 78 (2013).

[48] J. Lippuner and L. F. Roberts, Astrophys. J. **815**, 82 (2015).

[49] R. Fernández and B. D. Metzger, Mon. Not. Roy. Astron. Soc. **435**, 502 (2013).

[50] O. Just, A. Bauswein, R. A. Pulpillo, S. Goriely, and H.-T. Janka, Mon. Not. Roy. Astron. Soc. **448**, 541 (2015).

[51] M.-R. Wu, R. Fernández, G. Martínez-Pinedo, and B. D. Metzger, Mon. Not. Roy. Astron. Soc. **463**, 2323 (2016).

[52] D. M. Siegel and B. D. Metzger, Phys. Rev. Lett. **119**, 231102 (2017).

[53] R. Fernández, A. Tchekhovskoy, E. Quataert, F. Foucart, and D. Kasen, Mon. Not. Roy. Astron. Soc. **482**, 3373 (2019).

[54] A. Arcones and G. Martínez-Pinedo, Phys. Rev. C **83**, 045809 (2011).

[55] B. Côté, C. L. Fryer, K. Belczynski, O. Korobkin, M. Chruślińska, N. Vassh, M. R. Mumpower, J. Lippuner, T. M. Sprouse, R. Surman, and R. T. Wollaeger, Astrophys. J. **855**, 99 (2018).

[56] L. Phillips, R. Gatti, R. Brandt, and S. Thompson, J. Inorg. Nucl. Chem. **25**, 1085 (1963).

[57] C. J. Horowitz, A. Arcones, B. Côté, I. Dillmann, W. Nazarewicz, I. U. Roederer, H. Schatz, A. Aprahamian, D. Atanasov, A. Bauswein, T. C. Beers, J. Bliss, M. Brodeur, J. A. Clark, A. Frebel, F. Foucart, C. J. Hansen, O. Just, A. Kankainen, G. C. McLaughlin, J. M. Kelly, S. N. Liddick, D. M. Lee, J. Lippuner, D. Martin, J. Mendoza-Temis, B. D. Metzger, M. R. Mumpower, G. Perdikakis, J. Pereira, B. W. O'Shea, R. Reifarth, A. M. Rogers, D. M. Siegel, A. Spyrou, R. Surman, X. Tang, T. Uesaka, and M. Wang, J. Phys. G: Nucl. Part. Phys. **46**, 083001 (2019).

[58] A. Mamdouh, J. M. Pearson, M. Rayet, and F. Tondeur, Nucl. Phys. A **679**, 337 (2001).

[59] A. J. Koning, S. Hilaire, and M. C. Duijvestijn, TALYS-1.0, in *ND2007 - International Conference on Nuclear Data for Science and Technology* (EDP Sciences, Les Ulis, 2007), pp. 211–214.